Research Article

Finite Element Analysis and Simulation about Microgrinding of SiC

Shijun Ji, Leilei Liu, Ji Zhao, and Changrui Sun

School of Mechanical Science and Engineering, Jilin University, Changchun 130025, China

Correspondence should be addressed to Ji Zhao; jzhao@jlu.edu.cn

Academic Editor: Takuya Tsuzuki

The application of silicon carbide (SiC) is often limited due to its low machining efficiency and unpredictability about the results of the grinding process. The aim of this paper is to set up finite element analysis models (FEM) about microgrinding process of SiC, to study the change processes about tangential and normal grinding force which can lead to stress and strain inside SiC material under different grinding parameters, and to predict the results before the grinding process. Adaptive remeshing technique is used to minimize the computational time without sacrificing the accuracy of the results in the simulation of SiC grinding process. The research results can be used to choose reasonable grinding parameters based on the required surface quality.

1. Introduction

Due to its high strength, high hardness, and chemical stability at high temperatures, silicon carbide, as an advanced material, has attracted more attention and a wide range of applications, such as optical instrument, automotive, aerospace, and construction industry [1, 2]. In fact, considering the lightweight of the spatial optical system, SiC optical mirror can do well in spatial optical system and components [3].

As the abrasive is embedded inside the microgrinding tool, abrasive belt grinding has a longer life span than the electroplated one. In recent years, studies of surface generation and process optimization have been conducted about the microgrinding of ceramic materials on account of the above advantages [4–7]. The research of nanowires and brittle single crystal materials on brittle-to-ductile transition receives wide concerns and it is applied into other materials behaving brittle and ductile properties [8–10]. Doman, Barge, and Qiuning discussed the brittle-to-ductile transition and critical cutting depth by developing several single-grit models and conducting many experiments [11–13]. It is known that ductile-regime grinding is capable of attaining better surface

quality. However, due to the brittle nature and high hardness, postmachining will be difficult and increase the cost of SiC product significantly in the fabrication of parts with big size and complex shape. Furthermore, Wang et al. investigated the changes of grinding force influenced by the velocity in the grinding process [14]. Arrazola et al. have established several models and they do some experiments of other materials to study how the grinding geometrical shapes of tool affect the grinding results [15–19]. But fewer simulation models are successful owing to either lack of considering the nose radium or inability to establish steady-state models.

In this paper, the finite element method simulation based on the single point diamond turning (SPDT) technology is studied, and the simple variable method is adopted to analyze the effect caused by depth, velocity, and tool's parameters in microgrinding process. The main purpose is to generate the effective grinding simulation according to the given microgrinding parameters, which can forecast and optimize processing ahead of machining. To verify the finite element simulation of microgrinding process, experiments are conducted for scratching the SiC sample with different depths and velocities. This paper not only reports the performance

of SiC microgrinding process combined with geometrical parameters of tool but also provides a rational reference for practical manufacturing.

2. Description of Finite Element Model

2.1. Single Abrasive Grinding Principle. In order to generate SiC chip and cutouts in microgrinding process, it is necessary to consider the critical grinding depth. The cutting edge of abrasive can make the material flow and bulge in front and it can make the chips of the cut slide along the cutting edge. When the depth of microgrinding is less than the critical grinding depth, the chip of silicon carbide material is formed and removed in a manner of the plastic flow. Whereas the microgrinding depth is greater than the critical grinding depth, manufacturing process is brittle grinding. As shown in Figure 1, γ is the rake angle; α is the clearance angle; Φ is the shear angle; t is the initial microgrinding depth; I is the primary deformation zone; II is the second deformation zone; III is the third deformation zone.

2.2. Single Abrasive Finite Element Model of Microgrinding. In the study of microgrinding mechanism, the grinding process of SiC mirror can be simplified to the two-dimensional orthogonal microgrinding finite element analysis model. The hardness and modulus of elasticity of single diamond abrasive are far more than SiC workpiece, even though the machining process is elastic belt grinding. Therefore, abrasive grit is assumed to be analyzed rigid body during the simulation. As shown in Figure 2, the model size of SiC workpiece is 2 μm $\times$ 1.5 μm. Quadrilateral element mesh is generated by linear reduced integration unit (CPE4RT) and structured mesh technique, which is stable in the meshing process. Moreover, edge biased seed is applied to encrypt meshes in the region to be manufactured. In addition, improved Lagrange law (ALE) is adopted so that mesh distortion would be avoided in microgrinding process. Both accuracy of solving the premise and operational efficiency are taken into account.

2.2.1. Material Constitutive Model. Drucker and Prager model, proposed by Drucker and Prager, is chosen, in which the influence on the yield of hydrostatic pressure is considered. The yield function for the Drucker-Prager model is as follows:

$$f\left(I_1, \sqrt{J_2}\right) = \sqrt{J_2} - \alpha I_1 - k = 0, \qquad (1)$$

where I_1 and $\sqrt{J_2}$ are the invariant of the stress tensor. α and k are the material constant.

In Abaqus, coefficient of expansion δ can be represented by the expansion angle ψ

$$\delta = \tan\left(\psi\right),$$

$$\delta = \frac{\operatorname{tr} D^p}{\left(2D^{p'} : D^{p'}\right)^{1/2}}, \qquad (2)$$

where D^p is on behalf of the plastic of the deformation rate tensor D. $D^{p'}$ represents the deviation section of D^p.
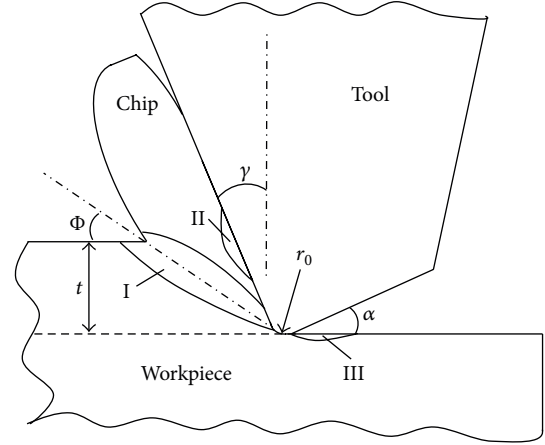

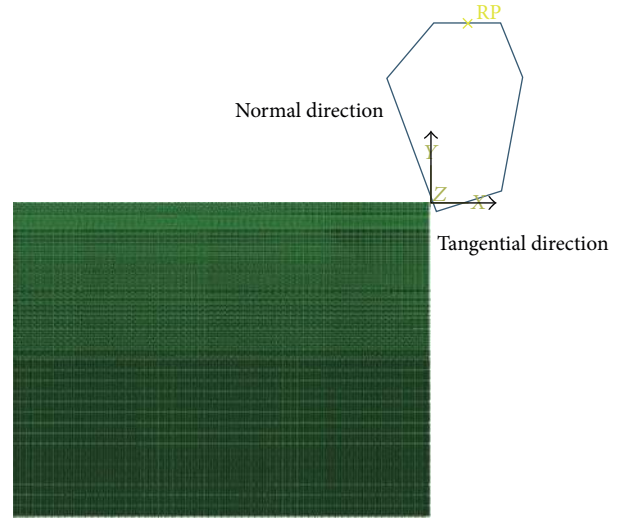FIGURE 1: Microgrinding process of abrasive.

FIGURE 2: Two-dimensional finite element model.

In Mohr-Coulomb model, the angle of internal friction can be obtained by single-yield tensile and compressive stress:

$$\phi = \sin^{-1}\left(\frac{\sigma_c - \sigma_t}{\sigma_c + \sigma_t}\right). \qquad (3)$$

By comparing the Mohr-Coulomb model with the linear Drucker-Prager model,

$$\tan\beta = \frac{6\sin\phi}{3 - \sin\phi},$$

$$K = \frac{3 - \sin\phi}{3 + \sin\phi}, \qquad (4)$$

where β is the slope of the linear yield surface in the p-t stress plane and is commonly referred to as the friction angle of the material. K is the ratio of the yield stress in triaxial tension to the yield stress in triaxial compression [20]. The specific parameter is shown in Table 1.
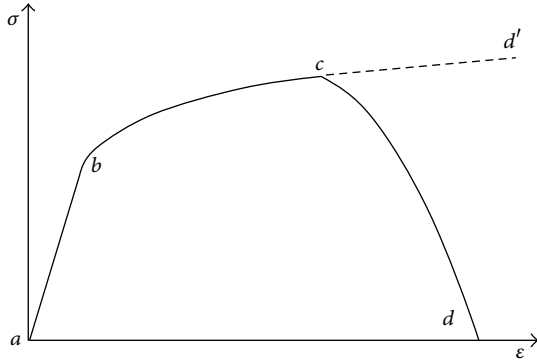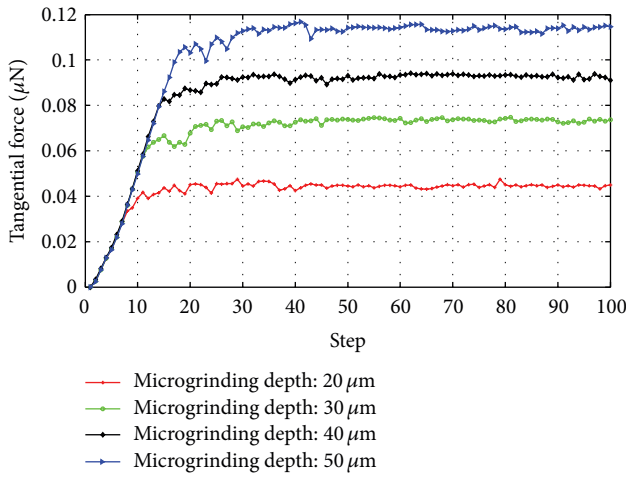
FIGURE 3: Yield diagrammatic sketch.

FIGURE 5: The normal force comparison for different depths.

FIGURE 4: The tangential force comparison for the different microgrinding depths.
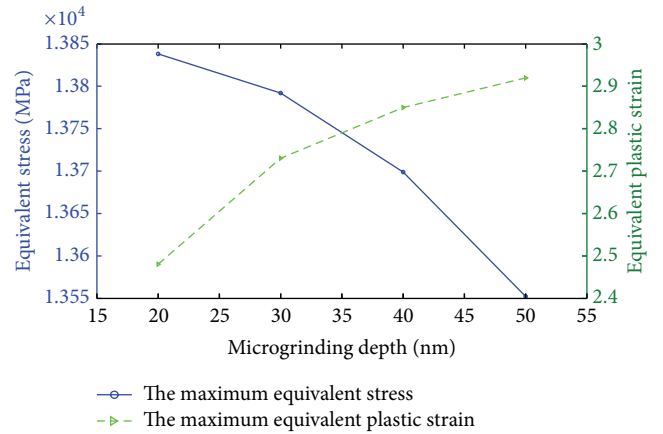
FIGURE 6: Changes of the equivalent stress and the equivalent plastic strain based on the depth.

TABLE 1: Constitutive model parameters of the SiC workpiece material.

Density (kg/m^3)	3250	Angle of friction (°)	13
Young's modulus (GPa)	205	Flow stress ratio	0.92
Poisson's ratio	0.16	Dilation angle (°)	−5
Thermal conductivity (J/m·K)	185	Yield stress (MPa)	12500
Expansion coefficient alpha (μm/K)	4	Specific heat (J/kg·K)	800

2.2.2. Chip Separation Criterion. The stress-strain response, as illustrated in Figure 3, shows distinct phases. The material response is initially linear elastic, *a-b*, followed by plastic yielding with strain hardening, *b-c*. Beyond point *c*, there is a marked reduction of load-carrying capacity until rupture, *c-d*. The deformation during this last phase is localized in a neck region of the specimen. Point *c* identifies the material state at the onset of damage, which is referred to as the damage initiation criterion. Beyond this point, the stress-strain response *c-d* is governed by the evolution of the degradation of the stiffness in the region of strain localization.
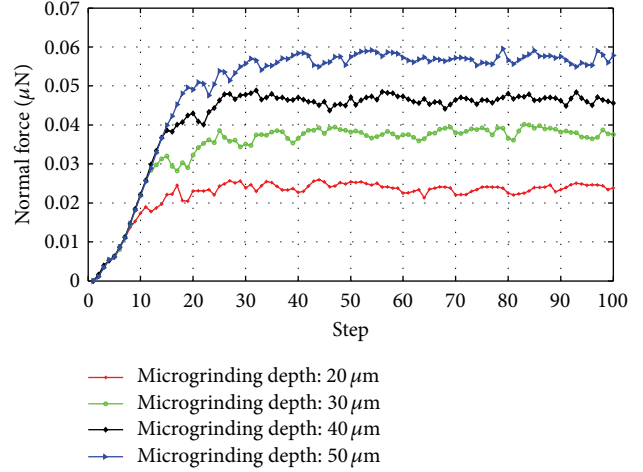
The criterion for damage initiation is met when the following condition is satisfied:

$$\omega_s = \int \frac{d\bar{\varepsilon}^{pl}}{\bar{\varepsilon}_s^{pl}} = 1, \tag{5}$$

where ω_s is a state variable that increases monotonically with plastic deformation proportional to the incremental change in equivalent plastic strain, $\bar{\varepsilon}_s^{pl}$ is the equivalent plastic strain, and $d\bar{\varepsilon}^{pl}$ is the equivalent plastic strain increment.

3. The Results of Finite Element Analysis

In the microgrinding progress, the force of microgrinding is affected by microgrinding depth, rake angle, clearance angle, microgrinding velocity, and the abrasive nose radius of cutting edge to different extent, and then the smooth grinding process changes, so that rough precision of microgrinding surface emerges. Now the influence of parameters of tool in simulation is studied in microgrinding process, and different models in simulation are shown in Table 2.
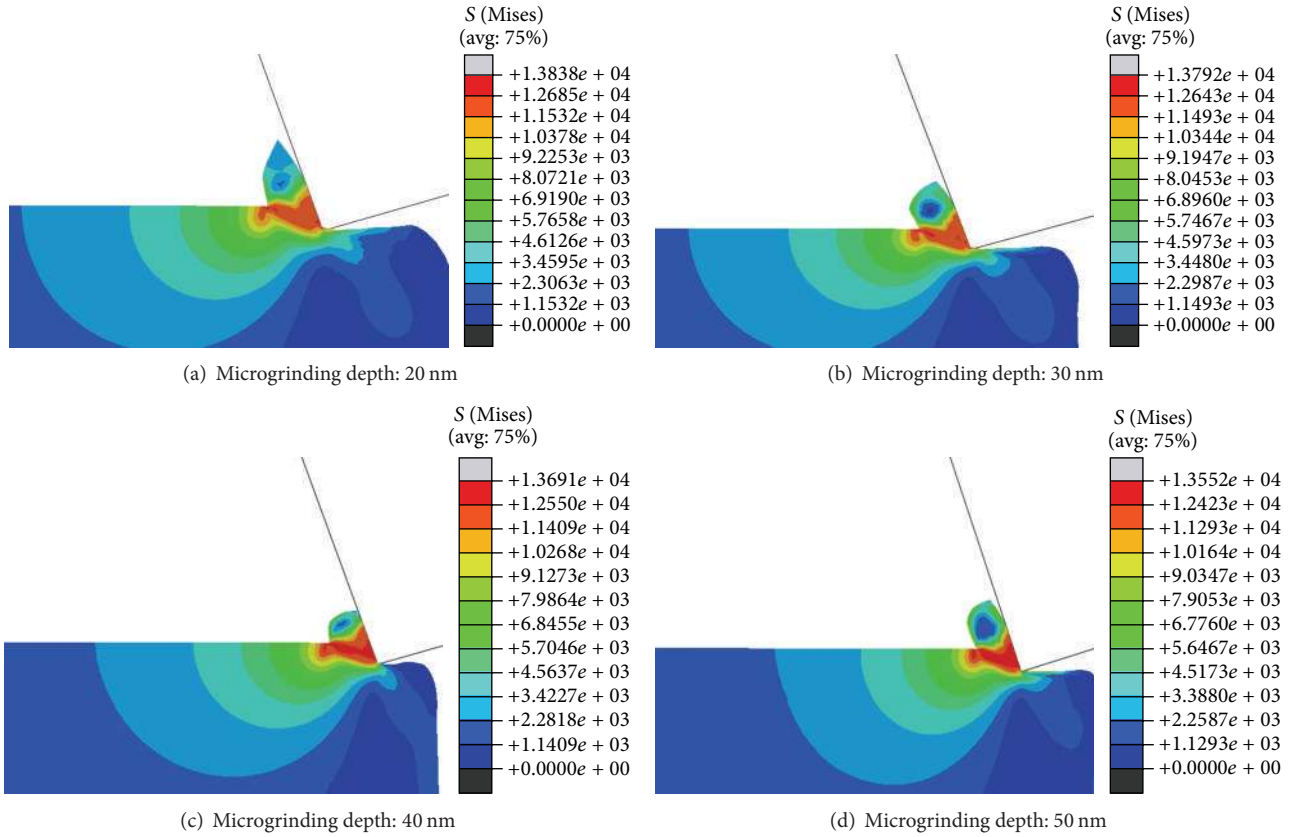
S (Mises)
(avg: 75%)

+1.3838e + 04
+1.2685e + 04
+1.1532e + 04
+1.0378e + 04
+9.2253e + 03
+8.0721e + 03
+6.9190e + 03
+5.7658e + 03
+4.6126e + 03
+3.4595e + 03
+2.3063e + 03
+1.1532e + 03
+0.0000e + 00

(a) Microgrinding depth: 20 nm

S (Mises)
(avg: 75%)

+1.3792e + 04
+1.2643e + 04
+1.1493e + 04
+1.0344e + 04
+9.1947e + 03
+8.0453e + 03
+6.8960e + 03
+5.7467e + 03
+4.5973e + 03
+3.4480e + 03
+2.2987e + 03
+1.1493e + 03
+0.0000e + 00

(b) Microgrinding depth: 30 nm

S (Mises)
(avg: 75%)

+1.3691e + 04
+1.2550e + 04
+1.1409e + 04
+1.0268e + 04
+9.1273e + 03
+7.9864e + 03
+6.8455e + 03
+5.7046e + 03
+4.5637e + 03
+3.4227e + 03
+2.2818e + 03
+1.1409e + 03
+0.0000e + 00

(c) Microgrinding depth: 40 nm

S (Mises)
(avg: 75%)

+1.3552e + 04
+1.2423e + 04
+1.1293e + 04
+1.0164e + 04
+9.0347e + 03
+7.9053e + 03
+6.7760e + 03
+5.6467e + 03
+4.5173e + 03
+3.3880e + 03
+2.2587e + 03
+1.1293e + 03
+0.0000e + 00

(d) Microgrinding depth: 50 nm

FIGURE 7: Comparison of the maximum equivalent stress.

TABLE 2: Models of the finite element simulation.

Group	Number	Microgrinding depth (nm)	Rake angle (°)	Clearance angle (°)	Nose radium of cutting edge (nm)	Velocity (m/s)
1	1	20	−20	16	5	1
	2	30	−20	16	5	1
	3	40	−20	16	5	1
	4	50	−20	16	5	1
2	1	40	−30	16	5	1
	2	40	−20	16	5	1
	3	40	−10	16	5	1
	4	40	0	16	5	1
3	1	40	−20	12	5	1
	2	40	−20	16	5	1
	3	40	−20	20	5	1
	4	40	−20	24	5	1
4	1	40	−20	16	5	1
	2	40	−20	16	10	1
	3	40	−20	16	15	1
	4	40	−20	16	20	1
5	1	40	−20	16	5	1
	2	40	−20	16	5	5
	3	40	−20	16	5	10
	4	40	−20	16	5	15

(a) Microgrinding depth: 20 nm

(b) Microgrinding depth: 30 nm

(c) Microgrinding depth: 40 nm
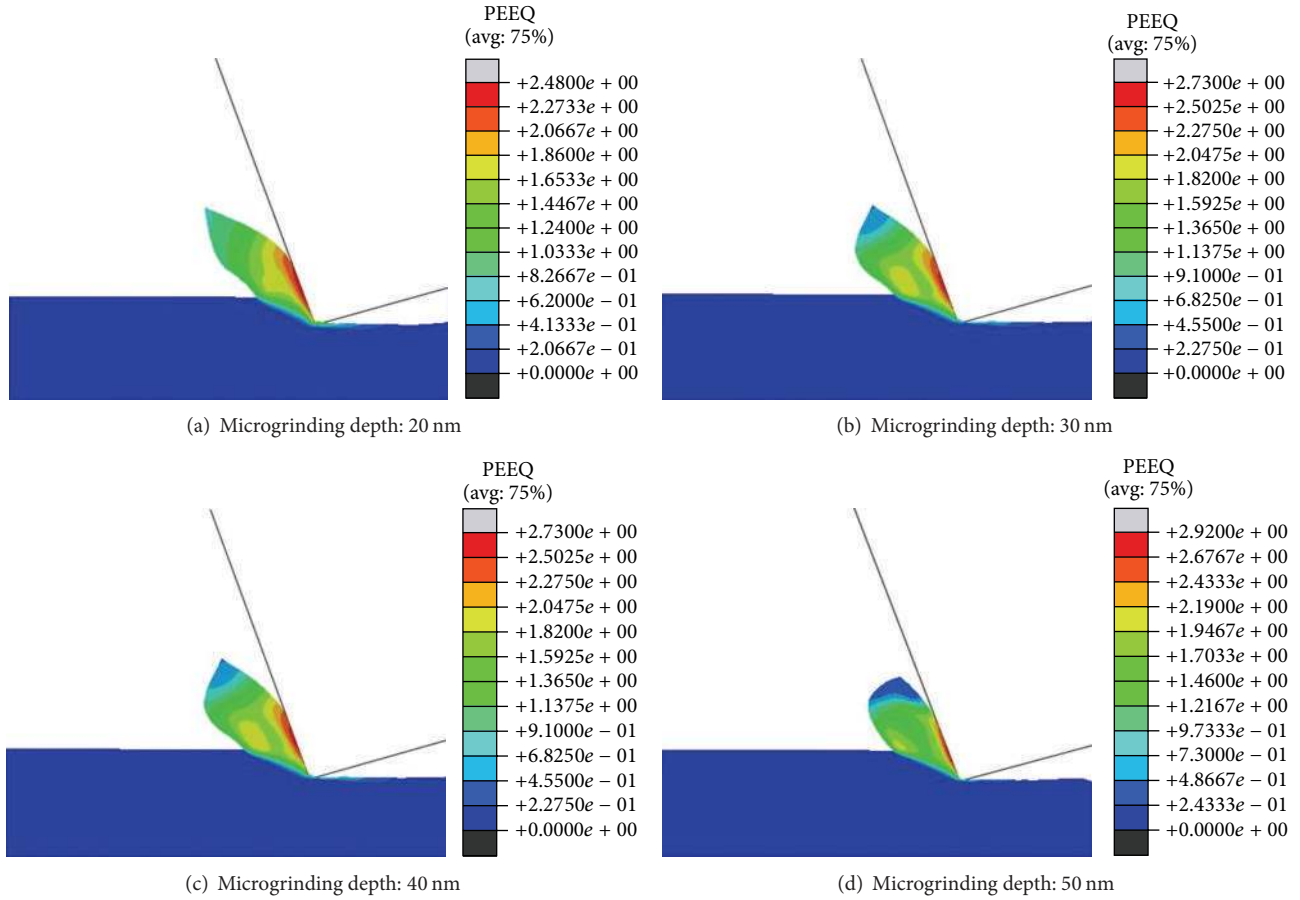
(d) Microgrinding depth: 50 nm

FIGURE 8: Comparison of the maximum equivalent plastic strain.

The third generation of mirror is made from SiC and carbon fiber reinforced SiC composites. SiC mirror has advantage in lightweight, whose radius-thickness ratio could reach 20 : 1 easily. The optical properties of SiC can be on a par with optical glass so that high polishing accuracy could be achieved [21]. As rough SiC surface would be achieved in the brittle machining process, the plastic processing is mainly studied in order to achieve higher precision SiC mirror. The critical microgrinding depth of SiC material is 65 nm; thus, several microgrinding depths of models in simulation are 20 nm, 30 nm, 40 nm, and 50 nm. As shown in Figure 4, the corresponding tangential forces are 0.04428 μN, 0.07368 μN, 0.09302 μN, and 0.1109 μN, respectively; and the homologous normal forces are 0.02376 μN, 0.03765 μN, 0.04647 μN, and 0.05758 μN, respectively. With the steady increase of microgrinding depth, the tangential force and the normal force rise stably. Due to the increase of microgrinding depth, undeformed chip thickens, and abrasive cutting area involved becomes bigger. Thus, the plastic deformation energy the abrasive needed to overcome and the grinding force grow bigger. Comparing the curve shape in Figure 4 with those in Figure 5, the tangential force is larger than the normal force in microgrinding process of identical depth. At the same time, the fluctuation of grinding force of group 1-model 4 whose microgrinding depth is 50 nm becomes bigger than the other models in group 1, resulting from the microgrinding

depth close to critical depth. The maximum equivalent stresses of group 1 are 13838 MPa, 13792 MPa, 13691 MPa, and 13552 MPa, respectively; and the maximum equivalent plastic strains are 2.48, 2.73, 2.85, and 2.92, respectively. As shown in Figure 6, with the increment of microgrinding depth, the maximum equivalent stress decreases successively, while the maximum equivalent plastic strain increases gradually. Figures 7 and 8 show that the maximum equivalent stress mainly emerges in the primary deformation zone and the second deformation zone, while the maximum equivalent plastic strain appears in the second deformation zone.

The theoretical formula of single abrasive grinding force [22]:

$$F_{tg} = \frac{\pi}{4} F_P \bar{a}_g^2 \sin \bar{\theta},$$

$$F_{ng} = F_P \bar{a}_g^2 \sin \bar{\theta} \tan \bar{\theta},$$

(6)

where $\bar{\theta}$ is semitip angle, $80° \leq 2\bar{\theta} \leq 140°$; $\bar{a}_g$ is undeformed microgrinding depth; F_p is unit microgrinding force:

$$F_{p1} = \frac{4F_{tg}}{\pi \bar{a}_g^2 \sin \bar{\theta}},$$

$$F_{p2} = \frac{F_{ng}}{\bar{a}_g^2 \sin \bar{\theta} \tan \bar{\theta}}.$$

(7)

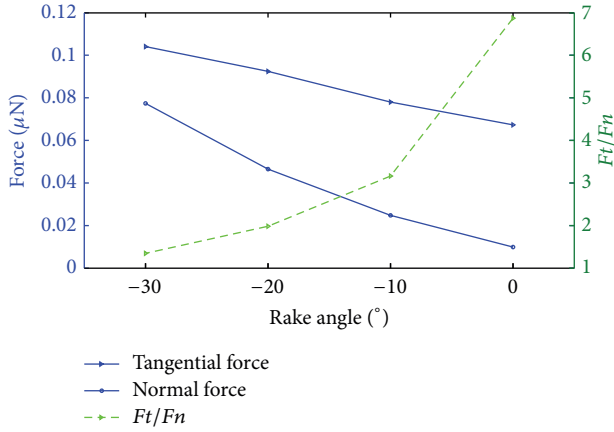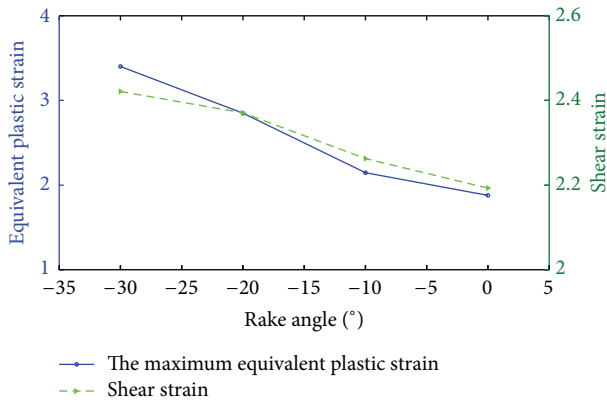FIGURE 9: Changes of grinding force based on rake angle.

FIGURE 11: Changes based on the clearance angle.

FIGURE 10: Changes of the strain based on rake angle.

FIGURE 12: Changes based on the nose radium of the cutting edge.

The average of F_{p1} and F_{p2} is adopted as F_p

$$F_p = \frac{F_{p1} + F_{p2}}{2}. \tag{8}$$

Taking the efficiency and accuracy of microgrinding into account, $\overline{a}_g$ is used as 40 nm. The unit microgrinding force can be calculated as approximate 8.44×10^7 N according to the simulation by Abaqus. The macroscopic force could be figured out simply after that.

Comparing the models in group 2, the result is shown in Figure 9. With the negative rake angle increasing steadily, the microgrinding force grows stably, while the ratio of the tangential force and the normal force of microgrinding F_t/F_n monotonically decreases. This is because the increment of the negative rake angle makes the contact area of abrasive and workpiece bigger, so does the load of abrasive cutting edge. The shear angles of the corresponding models are shown to be 32.89°, 27.50°, 23.37°, and 21.22°, respectively. The balanced augmenter of the negative rake angle gets the shear angle down. However, the cutting deformation changes conversely. Thus, the relation between the negative rake angle and the shear angle is consistent with Lee and Shaffer shear angle
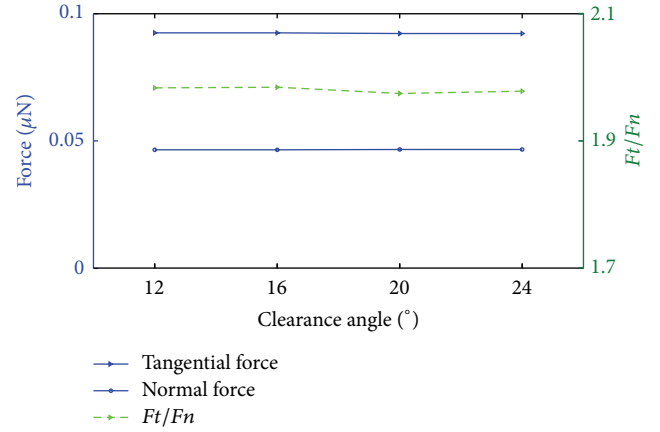
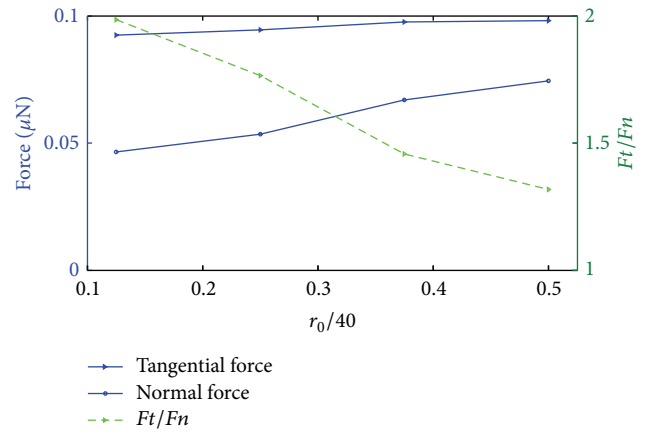theory [23]. Knowing the rake angle and the shear angle, the shear strain γ_0 can be further computed as follows:

$$\gamma_0 = \frac{\cos \gamma}{\sin \phi \cos (\phi - \gamma)}, \tag{9}$$

where γ is the rake angle of abrasive and Φ is the shear angle.

As shown in Figure 10, there is a rise of the maximum equivalent plastic strain and the shear strain along with the negative rake angle being larger. Furthermore, both alphabets of lines have the same trends.

With the clearance angle increasing gradually, the changing trends of the tangential force and the normal force are shown in Figure 11. The slight increase of the tangential force and the normal force can be negligible. What is more, the ratio of the tangential force and the normal force F_t/F_n almost has no change. In other words, the changes of clearance angle do not affect the stability of the machining process of SiC.

As shown in Figure 12, the elevation of the abrasive nose radium of cutting edge makes the microgrinding force become larger. Nevertheless, the tangential force has a small amplification, and the normal force has a big one. When the abrasive nose radium of cutting edge is far less than the microgrinding depth, the ratio of the abrasive nose radium
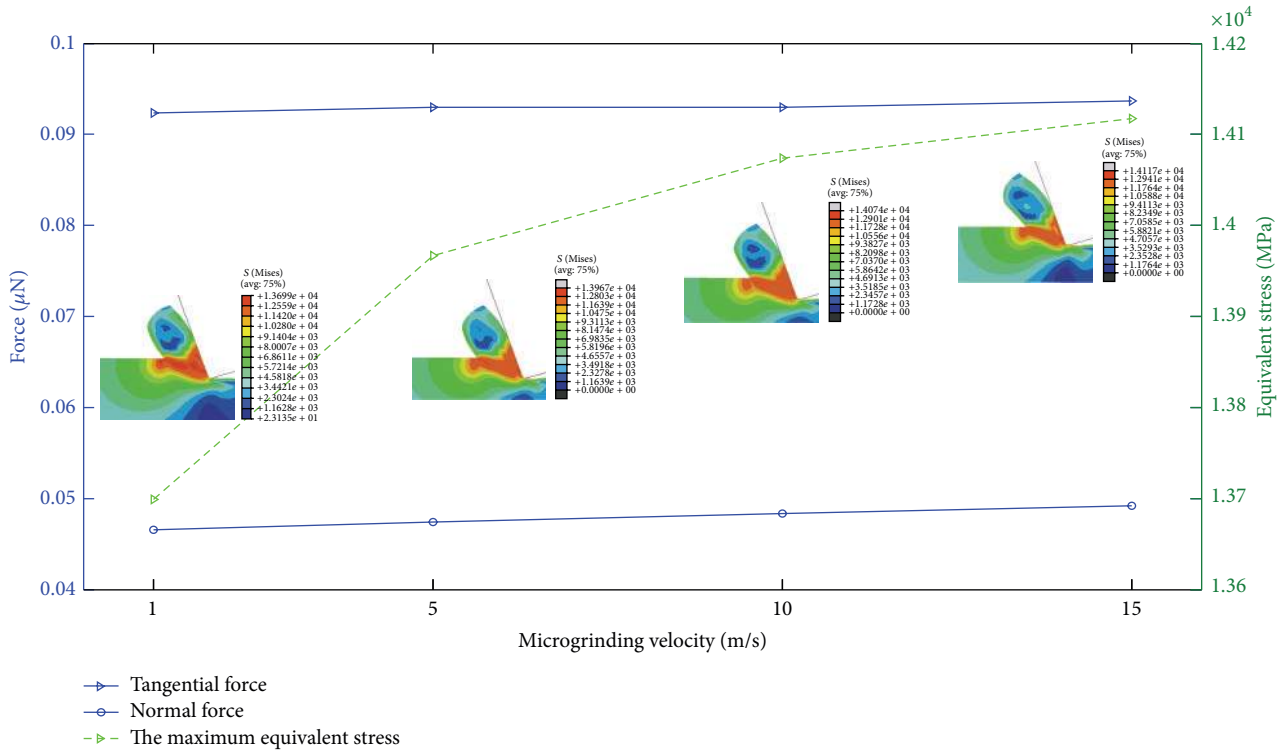
FIGURE 13: Changes based on microgrinding velocity.

of cutting edge and the microgrinding depth is nearly 0. Certainly, the changes of the abrasive nose radium of cutting edge do not affect the machining process of SiC. In other words, once the abrasive nose radium of cutting edge is at the same order of magnitude with the microgrinding depth, the nose radium of cutting edge can be ignored. In fact, the ratio of the tangential force and the normal force F_t/F_n is almost determined by the geometrical parameters of the abrasive, barely influenced by the microgrinding depth. Due to the rise of the nose radium of cutting edge, the ratio of the nose radium of cutting edge and the reference microgrinding depth $r_0/40$ ascends, whereas F_t/F_n comes down gradually.

As shown in Figure 13, with the velocity of microgrinding process increasing progressively, the tangential force and the normal force improve slightly, and both have weak increasing trends. The maximum equivalent stresses become 13699 MPa, 13967 MPa, 14074 MPa, and 14117 MPa, respectively. Considering the reduction of loss of machine tool and the perspective of energy conservation, 1 m/s is regarded as a good choice.

4. Experiments

According to the present limited research condition, to verify the validity of the above theoretical simulation model for the SiC microgrinding process, a series of scratch experiments have been conducted on the nanoindentation apparatus Agilent Nano Indenter G200 shown in Figure 14. And the scratch picture is given in Figure 15.

FIGURE 14: Agilent Nano Indenter G200.

In the experiments, simple variable method was adopted to observe the variation caused by microgrinding depth and the velocity. As to every depth and velocity, data of groups are obtained by the scratch experiments. Thus, the average load calculated in Table 3 could definitely give expression to the relationship between load and microgrinding depth.

After SiC workpiece polished finely, triangular pyramid head loading 1 mN scratched the SiC workpiece for 2 mm displacement, whose velocity is 1 mm/s. As the scratch improves from 20 nm to 30 nm to 40 nm to 50 nm, the load of triangular pyramid head reaches 0.0455 mN, 0.0463 mN, 0.0481 mN, and 0.0492 mN as illustrated in Figure 16. The normal force given in Figure 5 changes from 0.0238 μN to 0.0387 μN to 0.0471 μN to 0.0570 μN in simulation. Although the specific data is not in full consistency due to the situation

TABLE 3: Changes of load due to the depth and velocity.

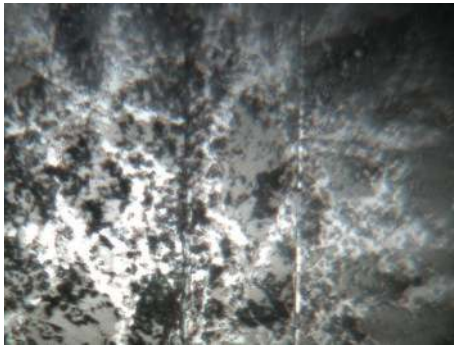| Simple variable method, depth (nm)	Load (mN)	Average load (mN)	Simple variable method, velocity (mm/s)	Load (mN)	Average load (mN)
20	0.0457 0.0450 0.0458	0.0455	1	0.0480 0.0486 0.0476	0.0481
30	0.0465 0.0462 0.0462	0.0463	5	0.0477 0.0473 0.0466	0.0472
40	0.0469 0.0491 0.0483	0.0481	10	0.0477 0.0476 0.0472	0.0475
50	0.0492 0.0495 0.0489	0.0492	15	0.0468 0.0476 0.0478	0.0474

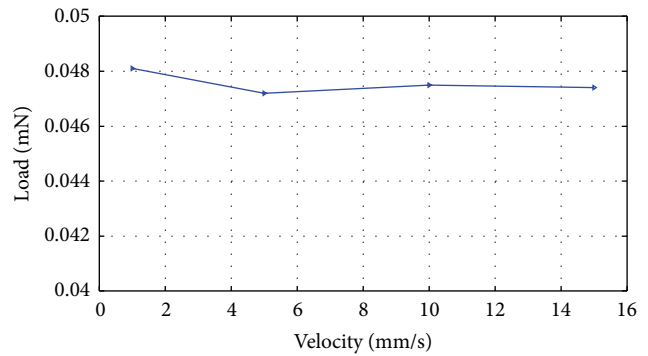

FIGURE 15: Scratched SiC workpiece.

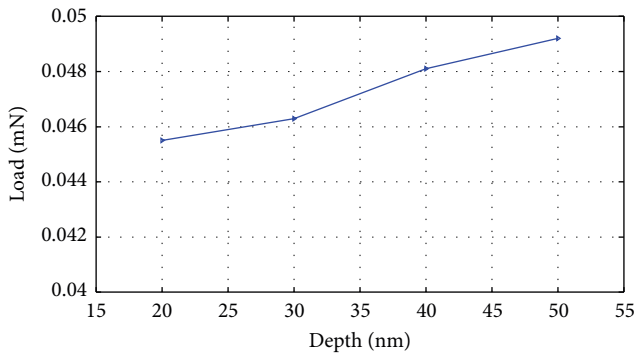FIGURE 17: Load change based on the velocity.

FIGURE 16: Load change based on the depth.

difference between the scratch and the grinding, both the experiment data and the simulation data show an obvious rising trend accompanied by the increase of scratch depth. In addition, a group of experiments, with same triangular pyramid parameters and 40 nm microgrinding depth, were implemented to indicate the effect of velocity. the nodes velocities in Figure 17 are 1 mm/s, 5 mm/s, 10 mm/s, and 15 mm/s, respectively, and the corresponding loads reach 0.0481 mN, 0.0472 mN, 0.0475 mN, and 0.0474 mN, respectively. At the same time, the normal force in simulation

achieves $0.0466\,\mu$N, $0.0474\,\mu$N, $0.0483\,\mu$N, and $0.0491\,\mu$N as shown in Figure 13. The data shown in the experiment and simulation vividly mean that triangular pyramid head load hardly goes with the change of velocity. Above all, good agreement is shown between the experimental results and the simulation results by Abaqus.

5. Conclusions

Based on the simulation of SiC microgrinding process presented in the paper, the following conclusions can be drawn.

(1) The depth of microgrinding plays a great role in the machining process. The process owns a 40 nm microgrinding depth having both small fluctuation and superior efficiency.

(2) For negative rake angle, a small one is a benefit to obtain the surface of SiC optical component.

(3) The clearance angle has barely an influence on the manufacturing of SiC surface in microgrinding process.

(4) To obtain a high accuracy of machining process, the abrasive nose radium of cutting edge needs to be compressed.

(5) Velocity of about 1 m/s is a proper choice in simulation of microgrinding process.

(6) Simulations of finite element in microgrinding process could provide a reference for the load in the coarse and fine grinding process of SiC mirror.
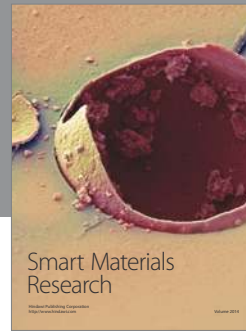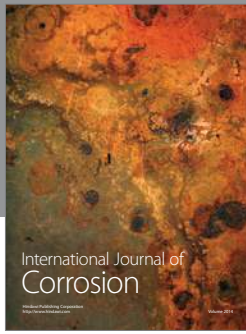
Conflict of Interests

The authors declare that there is no conflict of interests regarding the publication of this paper.

Acknowledgments

References

[1] R. Naslain, "Design, preparation and properties of non-oxide CMCs for application in engines and nuclear reactors: an overview," *Composites Science and Technology*, vol. 64, no. 2, pp. 155–170, 2004.

[2] W. Krenkel and F. Berndt, "C/C-SiC composites for space applications and advanced friction systems," *Materials Science and Engineering A*, vol. 412, no. 1-2, pp. 177–181, 2005.

[3] Y. Julong, *Ultraprecision Machining of Functional Ceramics*, Harbin Institute of Technology Press, Harbin, China, 2000.

[4] P.-H. Lee, H. Chung, and S. W. Lee, "Optimization of micro-grinding process with compressed air using response surface methodology," *Proceedings of the Institution of Mechanical Engineers, Part B: Journal of Engineering Manufacture*, vol. 225, no. 11, pp. 2040–2050, 2011.

[5] F. J. Chen, S. H. Yin, H. Huang et al., "Profile error compensation in ultra-precision grinding of aspheric surfaces with on-machine measurement," *International Journal of Machine Tools and Manufacture*, vol. 50, no. 5, pp. 480–486, 2010.

[6] J. Feng, B. S. Kim, A. Shih, and J. Ni, "Tool wear monitoring for micro-end grinding of ceramic materials," *Journal of Materials Processing Technology*, vol. 209, no. 11, pp. 5110–5116, 2009.

[7] J. Feng, P. Chen, and J. Ni, "Prediction of surface generation in microgrinding of ceramic materials by coupled trajectory and finite element analysis," *Finite Elements in Analysis and Design*, vol. 57, pp. 67–80, 2012.

[8] Z. Yuan, K.-I. Nomura, and A. Nakano, "A core/shell mechanism for stacking-fault generation in GaAs nanowires," *Applied Physics Letters*, vol. 100, no. 16, Article ID 163103, 2012.

[9] B. K. Tanner, M. C. Fossati, J. Garagorri et al., "Prediction of the propagation probability of individual cracks in brittle single crystal materials," *Applied Physics Letters*, vol. 101, no. 4, Article ID 041903, 2012.

[10] S. Goel, X. Luo, P. Comley, R. L. Reuben, and A. Cox, "Brittle-ductile transition during diamond turning of single crystal silicon carbide," *International Journal of Machine Tools and Manufacture*, vol. 65, pp. 15–21, 2013.

[11] D. A. Doman, *Rubbing and Plowing Phases in Single Grain Grinding*, Dalhousie University, Halifax, Canada, 2006.

[12] M. Barge, J. Rech, H. Hamdi, and J.-M. Bergheau, "Experimental study of abrasive process," *Wear*, vol. 264, no. 5-6, pp. 382–388, 2008.

[13] W. Qiuning, *Experimental study on single diamond grain grinding of silicon wafers [M.S. thesis]*, Dalian University of Technology, Dalian, China, 2006.

[14] J. Wang, R. Ye, and Y. Tang, "3D dynamic finite element simulation analysis of single abrasive grain during surface grinding," *Diamond & Abrasive Engineering*, vol. 173, no. 5, pp. 41–45, 2009.

[15] P. J. Arrazola and T. Özel, "Numerical modelling of 3D hard turning using arbitrary Lagrangian Eulerian finite element method," *International Journal of Machining and Machinability of Materials*, vol. 4, no. 1, pp. 14–25, 2008.

[16] M. Günay, I. Korkut, E. Aslan, and U. Şeker, "Experimental investigation of the effect of cutting tool rake angle on main cutting force," *Journal of Materials Processing Technology*, vol. 166, no. 1, pp. 44–49, 2005.

[17] Y.-C. Yen, A. Jain, and T. Altan, "A finite element analysis of orthogonal machining using different tool edge geometries," *Journal of Materials Processing Technology*, vol. 146, no. 1, pp. 72–81, 2004.

[18] H. Saglam, F. Unsacar, and S. Yaldiz, "Investigation of the effect of rake angle and approaching angle on main cutting force and tool tip temperature," *International Journal of Machine Tools and Manufacture*, vol. 46, no. 2, pp. 132–141, 2006.

[19] J. A. Badger and A. A. Torrance, "Comparison of two models to predict grinding forces from wheel surface topography," *International Journal of Machine Tools and Manufacture*, vol. 40, no. 8, pp. 1099–1120, 2000.

[20] ABAQUS, *User's Manual Version 6.6 Hibbitt*, Karlsson and Sorensen Inc, Proxidence, RI, USA, 2006.

[21] J. S. Johnson, K. D. Grobsky, and D. Bray, "Rapid fabrication of lightweight silicon-carbide mirrors," in *Proceedings of the International Symposium on Optical Science and Technology*, pp. 243–253, International Society for Optics and Photonics, 2002.

[22] B. Li and B. Zhao, *Modern Grinding Technology*, CMP, Beijing, China, 2003.

[23] E. H. Lee and B. W. Shaffer, "The theory of plasticity applied to a problem of machining," *Journal of Applied Mechanics*, vol. 18, pp. 405–413, 1951.

Journal of
Nanotechnology

International Journal of
Corrosion

International Journal of
Polymer Science

Smart Materials
Research

Journal of
Composites

BioMed
Research International

Journal of
Metallurgy

Journal of
Materials

Submit your manuscripts at
http://www.hindawi.com

Journal of
Nanoparticles

Advances in
Materials Science and Engineering

Scientifica

Journal of
Nanomaterials

**The Scientific
World Journal**

International Journal of
Biomaterials

Journal of
Nanoscience

Journal of
Coatings

Journal of
Crystallography

Journal of
Ceramics

Journal of
Textiles